Toward Mass-Production of Transition Metal Dichalcogenide Solar Cells: Scalable Growth of Photovoltaic-Grade Multilayer WSe_2 by Tungsten Selenization

Kathryn M. Neilson,[1†] Sarallah Hamtaei,[2,3,4†] Koosha Nassiri Nazif,[1†] Joshua M. Carr,[5] Sepideh Rahimisheikh,[6] Frederick U. Nitta,[1,7] Guy Brammertz,[2,3,4] Jeffrey L. Blackburn,[8] Joke Hadermann,[6] Krishna C. Saraswat,[1,7] Obadiah G. Reid,[8,9] Bart Vermang,[2,3,4] Alwin Daus,[1,10] and Eric Pop[1,7,11]

[1]*Dept. of Electrical Engineering, Stanford Univ., Stanford, CA 94305, USA*
[2]*Hasselt Univ., imo-imomec, Hasselt 3500, Belgium*
[3]*Imec, imo-imomec, Genk 3600, Belgium*
[4]*EnergyVille, imo-imomec, Genk 3600, Belgium*
[5]*Univ. Colorado Boulder, Materials Science & Engineering Program, Boulder CO 80303, USA*
[6]*Univ. Antwerp, Electron Microscopy for Materials Science (EMAT), Antwerpen 2020, Belgium*
[7]*Dept. of Materials Science & Engineering, Stanford Univ., Stanford, CA 94305, USA*
[8]*National Renewable Energy Laboratory, Chemistry and Nanoscience Center, Golden CO 80401, USA*
[9]*University of Colorado Boulder, Renewable and Sustainable Energy Institute, Boulder CO 80303, USA*
[10]*Sensors Laboratory, Dept. Microsystems Engineering (IMTEK), Univ. Freiburg, Freiburg, Germany*
[11]*Precourt Institute for Energy, Stanford Univ., Stanford, CA 94305, USA*

[†]*These authors contributed equally. *Corresponding author email: epop@stanford.edu*

ABSTRACT: Semiconducting transition metal dichalcogenides (TMDs) are promising for high-specific-power photovoltaics due to desirable band gaps, high absorption coefficients, and ideally dangling-bond-free surfaces. Despite their potential, the majority of TMD solar cells are fabricated in a non-scalable fashion using exfoliated materials due to the absence of high-quality, large-area, multilayer TMDs. Here, we present the scalable, thickness-tunable synthesis of multilayer WSe_2 films by selenizing pre-patterned tungsten with either solid source selenium at 900 °C or H_2Se precursors at 650 °C. Both methods yield photovoltaic-grade, wafer-scale WSe_2 films with a layered van der Waals structure and superior characteristics, including charge carrier lifetimes up to 144 ns, over 14× higher than any other large-area TMD films previously demonstrated. Simulations show that such carrier lifetimes correspond to power conversion efficiency of ~22% and specific power of ~64 W g^{-1} in a packaged solar cell, or ~3 W g^{-1} in a fully-packaged solar module. These results facilitate the mass-production of high-efficiency multilayer WSe_2 solar cells at low cost.

KEYWORDS: *transition metal dichalcogenides, solar cells, selenization, photovoltaic, carrier lifetime*

Semiconducting transition metal dichalcogenides (TMDs), e.g., MoS_2 and WSe_2, offer excellent electronic and optical properties for use in a variety of applications from nanoelectronics to photovoltaics. These include good charge carrier mobility in atomically thin (sub-1-nm) layers, ultrahigh optical absorption coefficients, near-ideal band gaps for solar energy harvesting, surfaces without dangling bonds, and facile integration on rigid and flexible substrates.[1-4] In particular, TMDs hold great promise in high-specific-power

(i.e. high-power-per-weight) applications, e.g., energy harvesting in high-altitude drones and wearable electronics, where light weight and high power output are desired.[5-7]These emerging photovoltaic markets are growing at a rapid pace, potentially exceeding $100B by 2027.[5]

Recent studies have shown that optimally-designed thin (<100 nm) TMD solar cells made of sulfides or selenides could achieve ~25% power conversion efficiency (PCE) in a single-junction structure[2, 8] and ~32% PCE in a TMD-silicon tandem structure,[9] on par with current perovskite-silicon tandem solar cells.[10] As a result, single-junction TMD solar cells can offer excellent specific power (power-per-weight) greater than 40 W g^{-1}, about 10× higher than established thin-film solar cell technologies cadmium telluride (CdTe), copper indium gallium selenide (CIGS), amorphous silicon (a-Si), and III-Vs.[6-7, 11] In addition, while thin-film solar cell technologies face challenges such as high cost (III-V single and multi-junction cells), low durability (perovskite, organic, dye-sensitized photovoltaics), and the use of rare (CIGS) or toxic materials (CdTe, PbS quantum dot, lead-based perovskite), TMD solar cells provide a potentially low-cost, durable, eco-friendly, and bio-compatible solution which could reach future large-scale adoption.

The majority of TMD synthesis research over the past decade has been focused on monolayer (< 1 nm) films, particularly for use in next-generation transistors. In contrast, high-quality TMD multilayers are most often obtained in a non-scalable fashion through the mechanical exfoliation of micron-scale flakes from bulk crystals grown by chemical vapor transport (CVT). Selenization, sulfurization, or tellurization of metallic precursor(s) could be employed as a low-cost method to synthesize TMD films at industrial scale, similar to CIGS.[12] In this approach, the substrate size is, in principle, limited only by the furnace dimensions and can be easily scaled to larger areas with the use of industrial tools.

In practice, while sulfurization has achieved more uniform films, selenization and tellurization have proven more difficult. This has been mainly attributed to a lower chemical reactivity of selenium and tellurium, which requires the presence of a reducing agent when growing selenide and telluride films.[13-14] While synthesis by tellurization has made progress,[14] the band gaps of semiconducting tellurium-based TMDs are smaller (~0.7 eV) and less optimal for solar applications than those of selenides. On the other hand, previous studies on selenization synthesis of WSe_2 films have displayed suboptimal properties for photovoltaics, being either too thin,[15-16] too rough,[17] and/or suffering from morphological inhomogeneity[18-19]. The selenization process itself could also exceed 20 hours, rendering it unfavourable from an industrial perspective.[20] An ideal film growth would have controllable thickness that is atomically smooth and oriented in the (001) direction, with sufficiently large grain sizes and good charge carrier lifetimes.

Herein, we demonstrate the scalable synthesis of multilayer (15-30 nm) WSe_2 on up to 150 mm wafers by selenization of sputtered tungsten films using 1) solid source selenium at 900 °C and 2) low-thermal-budget H_2Se precursors at 650 °C, in 1-2 hours, leading to optimal characteristics for use as an absorber

layer in ultrathin high-specific-power solar cells. At such thicknesses, WSe_2 has a band gap of 1.2-1.3 eV, which is near-ideal for solar energy harvesting under both AM0 and AM1.5G spectra. Additionally, our approach results in films with superior characteristics compared to previous selenization reports,[16-21] including van der Waals (vdW) layered structure, smooth and uniform surfaces, grain sizes comparable to the film thickness, Hall mobilities up to 8 $cm^2 V^{-1} s^{-1}$, and minority carrier lifetimes up to 144 ns, over 14× greater than previous reports on large-area TMD films prepared by liquid exfoliation.[19]. Here, we specifically focus on the absorber material due to the separate challenges associated with solar cell design;[22] however, with improved contacts and doping, these WSe_2 films can provide efficiency up to 22.3% in an optimized solar cell design. More importantly, upon integration on ultrathin flexible substrates, such solar cells are calculated to provide specific power of ~64 W g^{-1} in a packaged cell, over 10× higher than established thin-film solar cell technologies[11]. Fully packaged modules, which include considerations such as interconnect weight and encapsulation, show specific power of up to 3 W g^{-1}, approximately 5× higher than the record of 0.7 W g^{-1}, demonstrated in a multi-junction III-V-based solar module[5].

WSe_2 Growth by Selenization of Tungsten

To prepare the WSe_2 film, we sputter 5-10 nm of tungsten using a DC source (Kurt J. Lesker) at 50 W onto ~500 μm-thick silicon substrates at a pressure of 10 mTorr and an argon (Ar) flow rate of 50 sccm (**Fig. 1a**) to provide an optimal film porosity.[18] (See **Supplementary Fig. S1** for further discussion on the effect of sputtering pressure on growth quality.) These films can either be pre-patterned (via lithography and lift-off) or blanket-deposited. The tungsten films are then selenized into multilayer (15-30 nm) WSe_2 by either solid source selenization (SS-Se) at 900 °C or by hydrogen selenide (H_2Se) at 650 °C, as shown in **Fig. 1b-e**. The final film thickness is mainly controlled by the starting thickness of the sputtered W, with the caveat that very thin starting films (< a few nm) require significantly shorter growth times to remain as continuous films versus as islands. The growth rate is relatively consistent after a W thickness of a few nm, for a final film thickness of approximately 2.1 times the starting thickness. H_2Se provides a potentially more homogenous selenization and higher chemical reactivity, therefore lowering the synthesis temperature and thermal budget. SS-Se can be processed at higher temperatures with higher quality, but with more difficulty in process repeatability and scalability due to the use of solid source selenium pellets. Nevertheless, both routes have shown promise to produce large-area high-quality films in chalcogenide technologies (for example, CIGS[23-24]).

SS-selenization is carried out in a two-zone tube furnace (**Fig. 1b**) where Se pellets are placed in a crucible upstream, subsequently vaporized at elevated temperatures, then transported by carrier gas (Ar) to the main heating zone of the furnace containing the substrate. The substrate is placed face-down on a crucible to prevent sublimation of stoichiometric transition metal films at high temperatures,[25] and both zones are

heated to 400 °C for 20 minutes (**Fig. 1d**). Subsequently, the Se zone is heated to 550 °C and the substrate is heated to 900 °C for one hour. Given that the as-deposited W film may have natural surface oxidation before it is placed in the furnace, we flow additional H_2 gas to convert this surface into a more reactive WO_{3-x} form.[26] The furnace is then left to naturally cool down to room temperature.

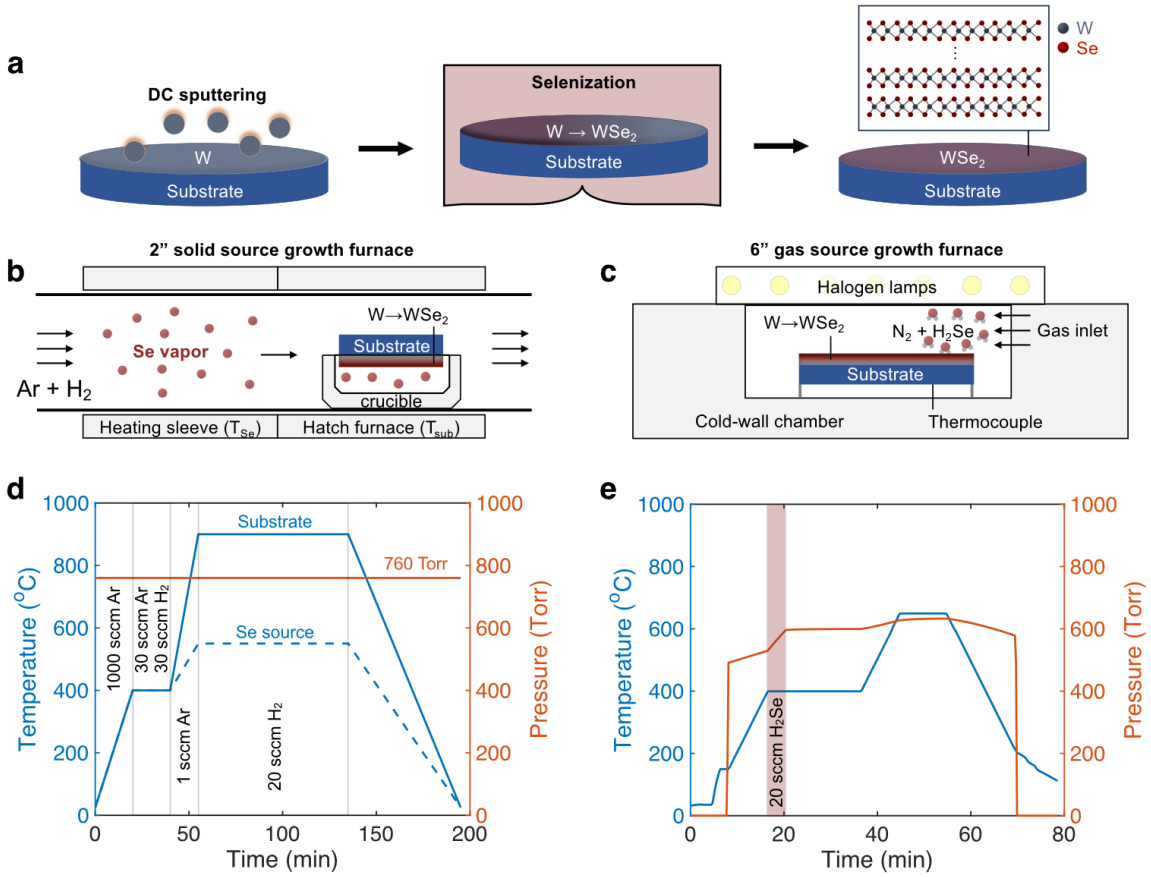

Fig. 1: Scalable growth of WSe_2 by selenization of tungsten (W) using solid source selenium (SS-Se) or H_2Se precursors. a, Selenization process flow. Furnace set-ups for **b,** SS-Se and **c,** H_2Se selenization processes. Optimized temperature and pressure vs. time for **d,** SS-Se and **e**, H_2Se processes. The dashed and solid blue lines in **d** correspond to T_{Se} and T_{sub} in **b**, respectively. H_2Se growth is done at a lower thermal budget (temperature) and pressure compared to SS-Se. Flow is continuously supplied for SS-Se (**d**) versus the finite introduction of H_2Se (**e**). Initial pressure changes in H_2Se growths are achieved by N_2 gas.

For the growth with H_2Se, a rapid thermal annealing tool is employed with N_2 and H_2Se as process gases (**Fig. 1c**). The sample faces up on a silicon carbide (SiC)-coated graphite susceptor. The growth is done by a two-stage anneal (**Fig. 1e**); the chamber is filled with 488 Torr of N_2 base pressure, which is then heated up to 400 °C. The sample is then annealed for 20 minutes, with 75 Torr of diluted H_2Se gradually fed into the chamber during the first 4 minutes, at 20 sccm. The flow rate is chosen to provide sufficient carrier gas, while allowing for the films to remain planar on the substrate (versus island formation or delamination *in situ*). The chamber is subsequently heated to 650 °C, where the sample is held for 10 minutes before

cooling to room temperature. Immediately after the two annealing stages (at 400 °C and 650 °C), the chamber pressure is 600 and 638 Torr, respectively. All heat-up and cool-down ramps are set to 0.5 °C/s.

Figure 2 shows the versatility and scalability of the selenization growth method. Selenization of W leads to multilayer WSe_2 films whose thickness can be tuned by the amount of sputtered W. The substrate size is only limited by the furnace dimensions, which in our study is 50 mm for the solid-source and 150 mm for the gas-source selenization (**Fig. 2a**). Industrialized furnaces would enable growth on even larger substrates, i.e. 300 mm or greater. The WSe_2 films are highly uniform, with van der Waals structure, and can be easily transferred to other rigid or flexible substrates, e.g. to build flexible, high-specific-power solar cells[11]. For example, **Fig. 2b** shows pre-patterned WSe_2 film transferred onto a flexible, lightweight polyimide substrate, and **Fig. 2c** demonstrates the growth uniformity on a 150 mm wafer by displaying the highest intensity Raman peak (E^1_{2g}) of WSe_2 normalized to the silicon substrate below.

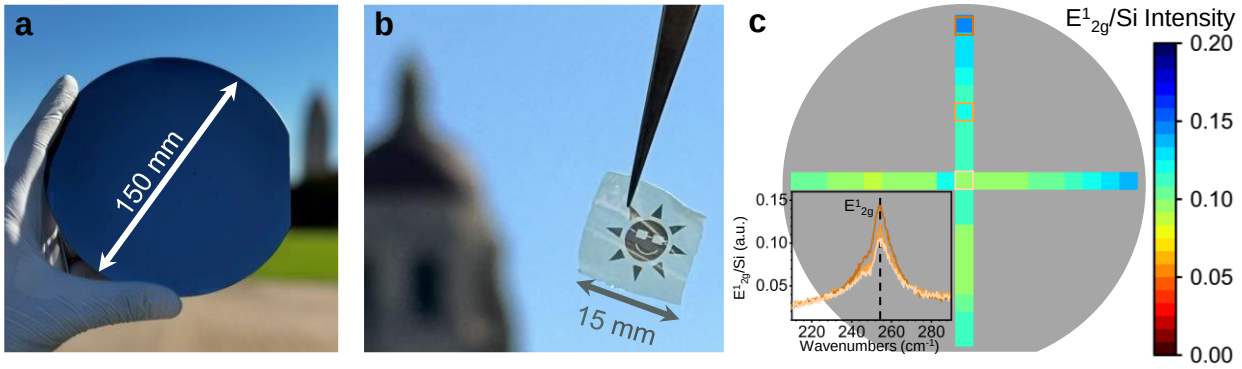

Fig. 2. Versatility and scalability of the selenization growth method. a, Photograph of a WSe_2 film uniformly grown by H_2Se on a 150 mm wafer. The film size is only limited by the substrate and furnace dimensions. **b,** WSe_2 film obtained from SS-Se selenization of pre-patterned W, transferred onto a flexible lightweight polyimide substrate. (Selenization can be performed both on blanket-deposited and patterned W.) Due to their van der Waals nature, such selenized films can be easily transferred to other rigid or flexible substrates. **c,** Raman spectroscopy shows little change of the E^1_{2g} peak intensity (normalized by the Si peak) over two orthogonal wafer diameters, indicating wafer-scale WSe_2 uniformity. Note that the measured data spans a narrower range (0.09-0.14) than the color bar (0-0.20), illustrating the growth uniformity. Inset shows normalized Raman spectra of the WSe_2 at three spots marked by squares along the vertical scan.

Material Characterization

Several characterization methods are used to assess the quality of the grown WSe_2 films. Initial scanning electron microscopy (SEM) images show smooth WSe_2 grown with H_2Se (**Fig. 3a**). Energy dispersive X-ray spectroscopy (EDS) is used to determine the Se to W ratio (**Fig. 3b-c**) of the films either as-grown on silicon or after transfer to PI. EDS spectra are taken under 5 kV acceleration voltage (**Fig. 3b**), to ensure data acquisition at the surface. The measurement is first done at the edge of the chip, as the smoothness of the films makes it difficult to focus near the center, followed by two more measurements at randomly chosen and wide apart locations.

Supplementary Table 1 summarizes the average and coefficient of variation between these three measurements on silicon (Si) and polyimide (PI) substrates for solid-source and H_2Se recipes, while **Fig. 3c** illustrates the average and standard deviation for Se and W values, as well as the Se:W ratio. For as-grown samples (on Si), there is a ~20% discrepancy between the compositions of solid-source and H_2Se recipes. This is mainly a measurement artifact caused by the proximity of W_M and $Si_{K\alpha}$ peaks at 1.774 and 1.739 keV, respectively, which causes peak fitting errors when translating the EDS peaks to atomic concentration. We avoid the Si peak by transferring WSe_2 films to a PI substrate. The EDS data from WSe_2 on PI substrates indicate very similar film compositions from each recipe (**Fig. 3c**), with a discrepancy of ~1% between the solid-source and H_2Se recipes, within the detection limit of EDS (1 atomic %). We also observe high spatial homogeneity for each recipe, with a coefficient of variation below 3% for Se and W atomic percentages (see tight error bars in **Fig. 3c**).

A transmission electron microscopy cross-section (**Fig. 3d**) confirms the van der Waals layered nature of the as-grown SS-Se films. Comparing the interlayer distances with the WSe_2 structure in the ICSD database ($a = b = 3.28$ Å, $c = 12.96$ Å, $\alpha = \beta = 90°$, $\gamma = 120°$)[27] and considering the atomic numbers of the constituting elements, each bright line is a plane containing W atoms, sandwiched between two Se layers (see **Fig. 3d**). The EDS result illustrated in **Fig. 3f and 3g** shows the elemental distribution in the lamella. Strong W and Se signals are seen atop the silicon substrate, confirming the elemental distribution in the film. Additionally, the lamella is smooth, as the atomic force microscopy (AFM) image shows a root mean square roughness on the order of 1 nm (**Fig. 3i**).

2θ-ω x-ray diffraction (XRD) scans verify the crystallinity of the selenized films, and the full-width at half-maximum is used to estimate the grain size using the Scherrer equation.[28] The presence of only (00ℓ) out-of-plane peaks for SS-Se WSe_2 in **Fig. 3h** demonstrates that the films are layered with alternating van der Waals gaps and undetectable out-of-plane crystallographic orientations, as verified by TEM (**Fig. 3d**). Estimates based on the Scherrer equation indicate grain sizes of ~17 nm for the SS-Se growth, comparable to the film thickness (see **Supplementary Note 1** and **Supplementary Table 2**). On the other hand, WSe_2 films prepared with H_2Se have smaller average grain sizes of ~8 nm, potentially due to the lower growth temperature and shorter anneal time (see **Fig. 1d-e**). Differences in the grain sizes of these films could be partially due to the higher synthesis temperature and longer anneal duration of SS-Se versus H_2Se (see Fig. **1d-e**); however, the role of the precursor and gas flow differences also contribute to film quality. While H_2Se films do show in-plane XRD peaks (**Fig. 3h**), further optimization of growth parameters (such as growth promoters, carrier gas, or pressure optimization) could provide more ideal film orientation, and larger grains, as the partial pressure of Se during growth can determine the film orientation.[20]

We also display Raman spectra of both selenization methods in **Fig. 3j**, normalized to the Si peak of the substrate. These provide information about the vibrational modes, which correlate with the relative quality of the films.[29] Solid source grown films exhibit a distinct degenerate A_{1g}/ E^1_{2g} peak and the 2LA(M) signature. H_2Se films show an increased left shoulder to the E^1_{2g} peak, which could be due to a higher presence of defects in these films[30] or to degenerate peak splitting due to an increased presence of strain,[31] as indicated by the shifted out of plane (00ℓ) peaks in the x-ray diffraction spectra (**Supplementary Table 2**).

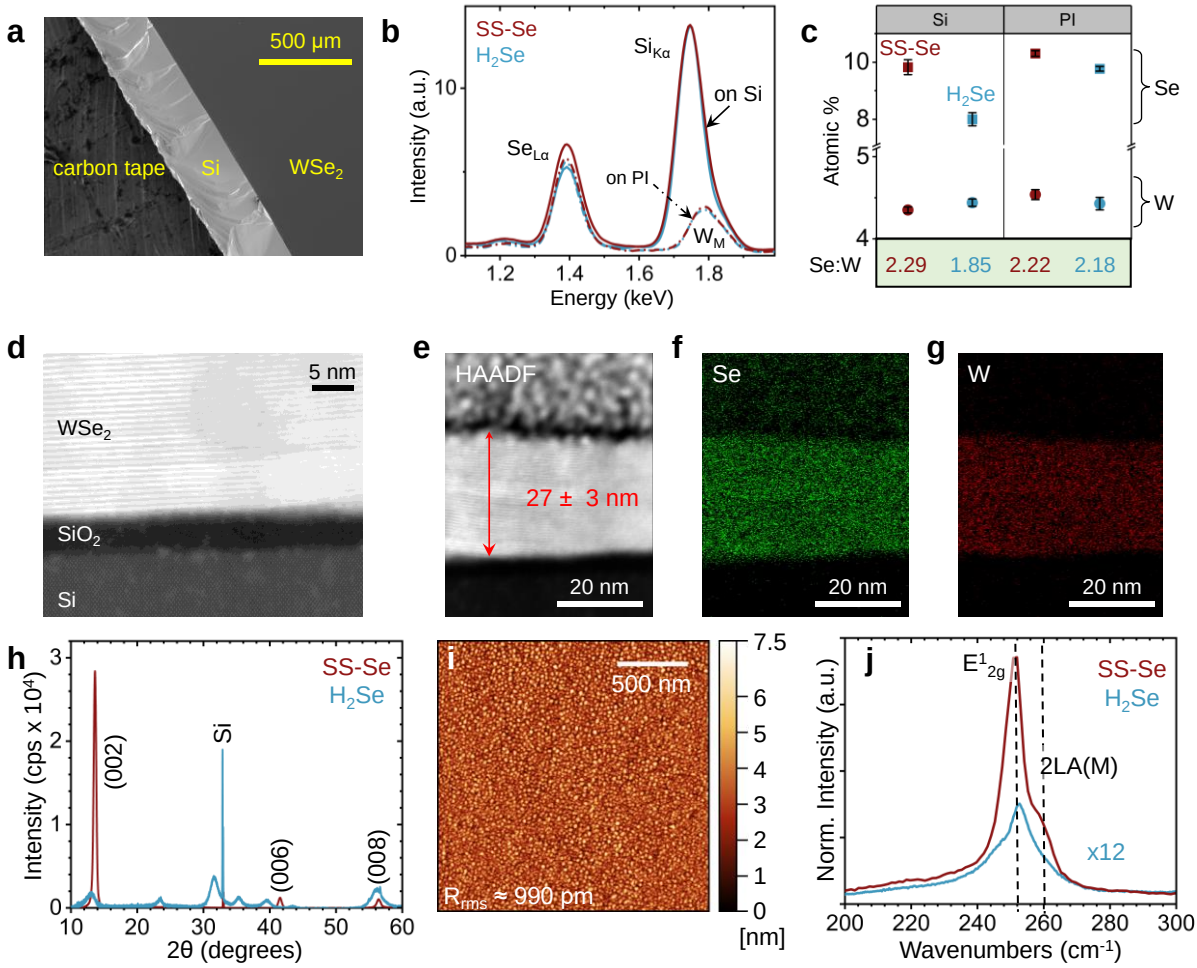

Fig. 3. Material characterization of WSe_2. a, H_2Se-grown films imaged under the scanning electron microscope (SEM) at the edge of the chip, **b,** resulting energy dispersive x-ray spectra of WSe_2 as-grown on Si and transferred onto polyimide (PI) in order to deconvolute the W emission from the Si substrate, **c,** resulting Se:W ratio of approximately 2:1, as anticipated for a fully-converted WSe_2 film. **d,** High angle annular dark field scanning transmission electron microscopy (HAADF-STEM) cross-section of WSe_2 samples from SS-Se growth. **e,** High-angle annular dark-field scanning TEM (HAADF-STEM) cross-section of the WSe_2 film with **f,** Se and **g,** W elemental mapping. The top layers are protective Pt/C coatings added during sample preparation. **h,** X-ray diffraction spectra of blanket films, measured on silicon. **i**, Film topography of H_2Se films measured by atomic force microscopy **j,** Room temperature Raman spectra of representative films on Si.

Square WSe_2 samples measured by the van der Pauw method are used to determine the majority carrier type, density, and their Hall mobility (fabrication details in **Supplementary Note 2)**. The films show p-type doping, with hole density ~10^{17} cm^3 and average Hall mobility of ~5 $cm^{-2}V^{-1}s^{-1}$ at room temperature (**Supplementary Fig. 4**). Across various samples, we measured Hall mobilities and hole densities up to 8 $cm^2\ V^{-1}\ s^{-1}$ and 4.2×10^{17} cm^{-3}, respectively. These are among the best mobility results reported to date for selenized WSe_2 (**Supplementary Table 2**). SS-Se samples exhibit a tight distribution of Hall mobility and hole density whereas H_2Se samples show wider variation (**Supplementary Fig. 4**). This could be explained by the mobility anisotropy in WSe_2 and the more varied orientation of WSe_2 layers observed in the H_2Se growths (**Supplementary Fig. 2**) causing sample-to-sample variation. In contrast, we note that SS-Se growths have better horizontal layering within the WSe_2 films.

Flash-photolysis time-resolved microwave conductivity (TRMC) measurement

The flash-photolysis time-resolved microwave conductivity (TRMC) method is adopted to determine the charge carrier lifetime in our selenized films, particularly as this dictates the efficiency limit in photovoltaic applications.[8] TRMC is a contactless microwave spectroscopy technique where a thin film sample is excited by a laser inside a resonant cavity, probed by microwave radiation, and measured as a function of time.[32] TRMC experiments provide the product of free-charge carrier yield and the sum of both electron and hole mobilities, known as the yield-mobility product $\phi \sum \mu = \phi(\mu_e + \mu_h)$, where ϕ is the yield of charges per photon, while μ_e and μ_h are the electron and hole mobility, respectively. Both electrons and holes are produced by photoexcitation, but the degree to which carriers experience trap sites (and the precise energies of those traps) is unclear to date, in TMDs. Thus, it is challenging to deconvolve $\phi \sum \mu$ to estimate the photogenerated carrier mobilities. Instead, we focus on the carrier lifetimes and report the yield-mobility product (normalized by the fraction of absorbed photons) for three excitation wavelengths.

To characterize TMD photoconductivity, we first examine the optical absorption and steady-state microwave conductivity (SSMC) action spectra[32-38] associated with films for which we could measure a sufficiently good response at low photon fluences (**Supplementary Fig. 5** and **Supplementary Fig. 6**). The optical absorption and SSMC action spectra provide the three excitation wavelengths (at 500, 580, and 780 nm) for the TRMC study, as follows: 1) bulk transitions above the WSe_2 band gap (500 nm or 2.48 eV), 2) transitions into the B exciton (580 nm or 2.14 eV), and 3) transitions into the lowest A exciton (780 nm or 1.59 eV).[39] **Figures 4a-c** display TRMC transients at varying fluences for the SS-Se films, at the three excitation wavelengths. **Figures 4d** and **4e** show the peak $\phi \sum \mu$ vs. fluence and the amplitude-weighted average carrier lifetimes vs. photon fluence, respectively. **Figure 4f** displays carrier lifetimes in WSe_2 films obtained from both SS-Se (red) and H_2Se (blue) growth methods at a fluence of $10^9\ cm^{-2}$, representing AM 1.5 G solar illumination. (The lifetimes are extrapolated from the average plateaus at low fluence in **Fig. 4e**.)

The data summarized in **Fig. 4d** and **4e** show that both the yield-mobility product and the carrier lifetimes depend on fluence for the 500 nm and 580 nm excitations, but the excitation at 780 nm yield less fluence-dependence. This is explained by the different initial excitation energies with respect to the WSe_2 band gap, i.e. the bulk and B exciton energies (2.48 and 2.14 eV, i.e. 500 and 580 nm) are above the WSe_2 optical gap (1.59 eV or 780 nm) and have overall lower Coulomb binding energies. Higher energy excitations (580 nm vs. 780 nm, **Fig. 4d**) lead to a greater yield of free charges, assuming the mobility is equal in both cases. This trend suggests either that the exciton binding energy decreases as the excitation energy increases, or that the relaxation process from higher energies to the minimum optical transition allows for more excitons to dissociate. However, the 500 nm excitations produce charges with a longer lifetime than 580 nm, despite their higher charge density. This unusual trend in lifetime could be due to defect sites facilitating charge separation, which are only made accessible by higher energy excitations, meaning that different types of defects could dominate the 500 nm vs. 580 nm charge separation and recombination.

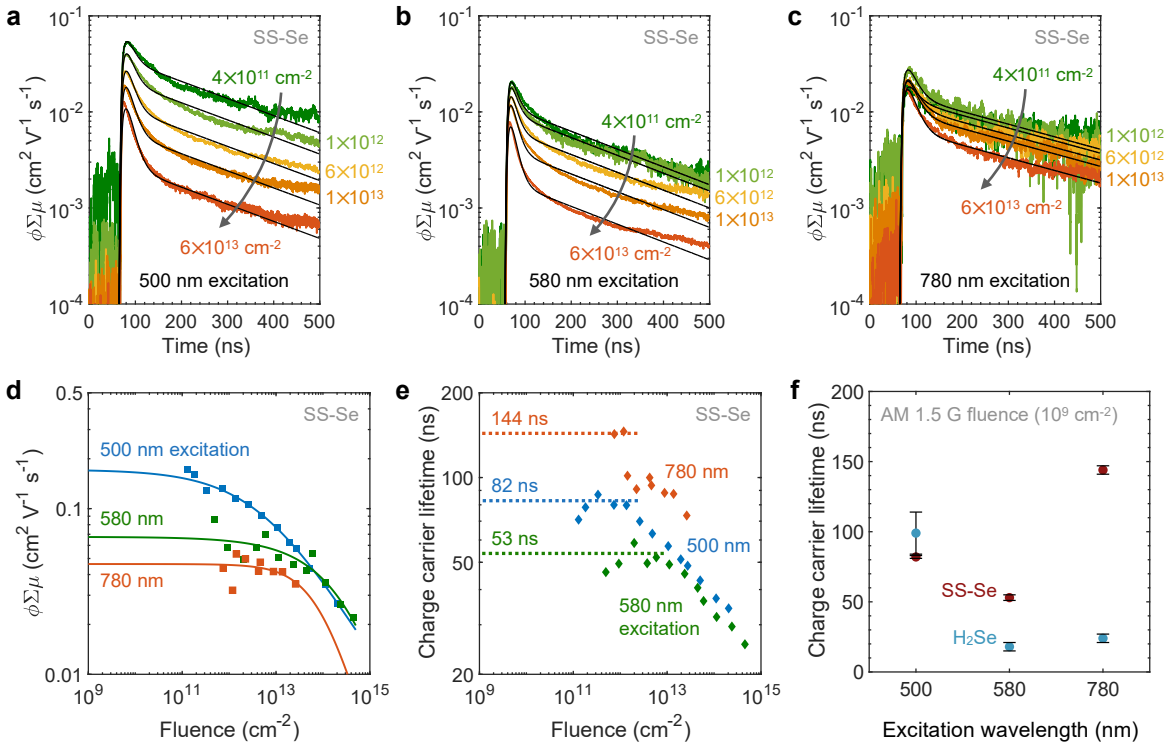

Fig. 4. Flash-photolysis time-resolved microwave conductivity (TRMC) measurements. TRMC transients of WSe_2 grown by SS-Se at varying photon fluences (from ≈ 10^{11} to 10^{14} cm^{-2}) for excitation wavelengths of **a**, 500 nm**, b,** 580 nm, and **c,** 780 nm. Some transients are omitted for clarity. Solid lines represent a double exponential fit to the data. **d**, Peak yield-mobility product vs. fluence at three excitation wavelengths (500, 580, and 780 nm) for WSe_2 grown by SS-Se. Square symbols are measurements; solid lines show a Dicker-Ferguson fit[40,41] to each data set, accounting for high-order recombination from exciton-exciton and exciton-charge quenching mechanisms. **e**, Amplitude-weighted average charge carrier lifetime vs. photon fluence at the same excitation wavelengths. Diamond symbols are measurements; dashed lines indicate charge carrier lifetimes averaged at low fluence, representing AM 1.5 G solar illumination (10^9 cm^{-2}).

f, Charge carrier lifetimes under AM 1.5 G fluence vs. the three excitation wavelengths, for WSe_2 films prepared by SS-Se (symbols in Stanford Cardinal red) and H_2Se (imec blue) selenization. Error bars are approximated as standard deviation of carrier lifetimes in the flat, plateaued regions of panel **e**.

As shown in **Fig. 4f**, SS-Se films tend to have higher carrier lifetimes than H_2Se samples, these results being the first of their kind in selenized WSe_2 films, to our knowledge. This could be related to the larger grain size in WSe_2 films grown by SS-Se (17 nm vs. 8 nm, see **Supplementary Table 2**). Selenization on textured substrates, such as in CIGS,[42] may allow for even larger grain sizes and subsequently larger lifetimes. The carrier lifetime of 144 ns measured in this work is over 14× higher than previous demonstrations of scalable, large-area TMD films (up to 10 ns in liquid exfoliated WS_2),[19] as shown in **Fig. 5a**. Our large carrier lifetimes can be attributed to the vdW layered structure and large grain size of our selenized films. Carrier lifetimes demonstrated here are on the same order of magnitude as the highest value reported for multilayer TMDs (611 ns for WS_2 grown by chemical vapor transport,[7] a non-scalable synthesis method), as well as more established chalcogenides CdTe and CIGS,[43-44] confirming the high quality of our synthesis, particularly for photovoltaic applications (**Fig. 5a**).

Projected efficiency and specific power of WSe_2 solar cells and modules

The ultimate performance limit of a single-junction solar cell is governed by the optoelectronic characteristics and synthesis quality of its absorber material. We perform a realistic modeling of single-junction solar cells performance limits with WSe_2 absorber layers by accounting for both intrinsic and extrinsic properties (**Fig. 5)**. The model incorporates measured absorption data as well as radiative, Auger, and defect-assisted Shockley-Read-Hall (SRH) recombination, as described in detail in our previous work[8].

Figure 5b shows the simulated current density vs. voltage and power conversion efficiency (PCE) limit of single-junction solar cells with 26 nm-thick WSe_2 absorber layers at various film quality levels, as represented by SRH recombination lifetimes (τ_{SRH}). This thickness is chosen here because it is that of our selenized films, and is the thickness which maximizes PCE[8] for lifetimes in the 10 ns to 1 μs range. Our model shows that τ_{SRH} of 10 ns, 100 ns, and 1 μs lead to PCE limits of 18.2%, 21.7%, and 25.1%, respectively (**Fig. 5b**). In the absence of SRH recombination (defect-free WSe_2, $\tau_{SRH} = \infty$), these 26 nm thin WSe_2 solar cells reach a PCE of 29.5% at the Tiedje-Yablonovitch limit (or up to ~30.8% in films thicker than 100 nm[8]). Carrier lifetimes associated with radiative and Auger recombination in intrinsic or lightly-doped multilayer WSe_2 are on the order of tens of micro-seconds.[8] Thus, measured carrier lifetimes below 1 μs correspond to SRH dominating recombination, which is the case for our selenized WSe_2 films (**Fig. 4f**). According to our realistic model, the selenized WSe_2 films in this study, which exhibit τ_{SRH} up to 144 ns, can achieve a PCE

of 22.3% (**Supplementary Table 3**) upon design optimization, which is on par with incumbent solar technologies such as Si, CdTe, and CIGS.[5]

More notably, after integration on ultrathin flexible substrates, selenized WSe_2 solar cells are expected to provide specific power of ~64 W g^{-1} in a packaged cell (**Fig. 5c**), over 10× higher than established thin-film solar cell technologies such as III-Vs, CdTe and CIGS.[11] These packaged WSe_2 solar cells could be adopted in size-constrained, low-power applications such as Internet of Things (IoT) and wearable electronics. Higher-power applications such as satellites and electric vehicles require larger, fully-packaged modules, with higher areal weight densities due to additional interconnects and module encapsulation.[5] Such fully-packaged WSe_2 modules have specific power of up to 3 W g^{-1}, over 4× higher than the present record of 0.7 W g^{-1} in multi-junction III-V solar modules.[5]

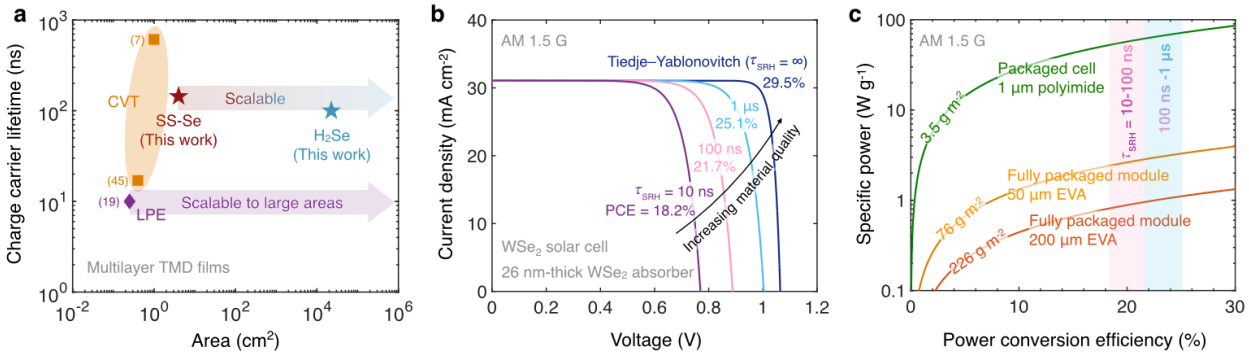

Fig. 5. Projected performance of WSe_2 solar cells and modules. a, Charge carrier lifetime and area of multilayer TMD films reported in the literature.[7, 19, 45] WSe_2 films grown by SS-Se and H_2Se selenization methods exhibit charge carrier lifetime up to 144 ns, over 14× higher than liquid phase exfoliation (LPE) and on par with chemical vapor transport (CVT). Note that CVT method is not scalable to large areas (maximum crystal size of ~1 cm^2), whereas both selenization and LPE could be scaled. **b,** Simulated current density vs. voltage characteristics and power conversion efficiency (PCE) limits of 26 nm-thick WSe_2 solar cells at various synthesis quality levels, represented by SRH recombination lifetime (τ_{SRH}). Our selenized WSe_2 films have carrier lifetime up to 144 ns, corresponding to a PCE of 22.3% in an optimized design (**Supplementary Table 3**). **c,** Projected specific power of WSe_2 solar cells and modules. Upon integration on ultrathin flexible substrates, selenized WSe_2 solar cells can provide specific power of ~64 W g^{-1} in a packaged cell, over 10× higher than established thin-film technologies.[11] Fully-packaged modules, which account for interconnect weight and EVA (ethylene-vinyl acetate) encapsulation,[5] show specific power up to 3 W g^{-1}, over 4× higher than the present record of 0.7 W g^{-1} in a multi-junction III-V based solar module.[5]

Conclusion

We report scalable methods for large-area WSe_2 film synthesis with both solid-source and gaseous precursors, for use as absorber layers in ultrathin high-specific-power solar cells. The films show van der Waals layered structure and grain sizes on the order of the film thickness (17 nm). We report some of the highest Hall mobilities to date, up to 8 $cm^2 V^{-1} s^{-1}$, in uniform, wafer-scale, multilayer films. These films also

have charge carrier lifetimes up to 144 ns, or 14× higher than previous reports on large-area TMDs. Simulations show that such lifetimes can lead to solar cell efficiency of ~22.3%, and specific power of ~64 W g^{-1} in a packaged cell or 3 W g^{-1} in a fully-packaged module. These results facilitate large-scale, commercial TMD solar cells with high specific power, which could address the growing need for lightweight, flexible energy harvesters for applications in IoT, wearables, electric vehicles, and aerospace.

Methods

Growth. Solid source selenium selenization was carried out in a two-zone PlanarTech CVD system, with the primary zone consisting of a hatch furnace and the second heating zone of an insulating jacket with heating coils in order to vaporize the solid source selenium.

Gas source selenization was done in a cold-wall rapid thermal processing furnace (Annealsys AS-One 150), capable of housing 150 mm wafers. The heat is provided by infrared halogen lamps on the chamber's lid, and the temperature is monitored using a thermocouple attached to the susceptor. Processing gases were nitrogen, and 10% diluted H_2Se in N_2.

TEM. To study the cross-section of the samples, a FIB lamella was prepared from each sample on a Cu Omniprobe TEM grid, using a Thermo Fisher Helios FIB-SEM and for characterization. High Angle Annular Dark Field Scanning Transmission Electron Microscopy (HAADF-STEM) and Energy Dispersive X-ray spectroscopy (EDS) were performed on an aberration-corrected Thermo Fisher Titan transmission electron microscope at 300 kV, using a Super X detector. To prevent damage from the ion beam on the sample, the surface was covered with a carbon-platinum layer and afterward coated with platinum.

Raman. Raman spectroscopy was taken using a HORIBA LabrRAM HR Evolution spectrometer using a laser wavelength of λ = 532 nm at P = 0.5 mW and at 1800 gr/mm, unless otherwise specified.

AFM. Atomic force microscopy is taken with a Park NX-10, using an NSC-15 tip at scan rate of 0.75 Hz.

XRD. X-Ray Diffraction is carried out with a PANAnalytical X'Pert 2 Diffractometer with a Cu-Kα source. Samples are first aligned to the (400) silicon peak to ensure orientation in the *z* direction, then measured using Cu-Kα radiation through a ½" slit without a parallel plate collimator.

TRMC. The detailed process for producing a quantitative measurement from TRMC is given in detail in our previous work, Reid *et al.*[32]

Specific power calculation: The specific power is calculated based on the solar cell efficiency and the areal weight densities of the solar cell or the module. The output power is equal to efficiency multiplied by the incident power of 100 mW cm^{-2} (AM 1.5 G one-sun illumination), and specific power is equal to the output

power divided by the areal density. The areal density of the packaged cell is calculated by summing up the areal densities of all materials in the packaged solar cell stack by using the volumetric mass density multiplied by the respective material thickness, as explained in detail in our previous study.[11] A material stack of 1 µm polyimide (substrate), 80 nm gold (back contact/reflector), 26 nm WSe_2 (absorber), single-layer graphene (top contact), and 70 nm MoO_x (anti-reflection coating/encapsulation layer) is considered as an example device structure.[11] The areal densities of the packaged modules are taken from the literature.[5] The values correspond to a lightweight, all-plastic packaging compatible with moisture-insensitive, thin-film solar technologies.

Contributions

K.M.N., S.H., and K.N. contributed equally. K.M.N., S.H., K.N. and A.D. conceived the project. K.M.N. and S.H. performed the growth of WSe_2. S.H. carried out the SEM and EDS measurements on WSe_2 films. S.R. performed the TEM and subsequent EDS measurements. K.M.N. performed Raman, XRD, and AFM characterization of the films. K.N. fabricated the devices and conducted the Hall measurements. K.N. and F.U.N. modeled the solar cell performance. K.N. did the specific power calculations. J.C., J.B. and O.R. conducted the TRMC measurements. K.M.N., S.H., and K.N. wrote the manuscript, with assistance from A.D., J.C., S.R., and E.P. E.P. supervised the work. All authors contributed to the data interpretation, presentation, and revision of the manuscript.

Supporting Information

Raman data for varying W sputtering conditions; elemental analysis of WSe_2 films; TEM of H_2Se films with elemental analysis; fit parameters from XRD; Hall measurements of SS-Se and H_2Se WSe_2; benchmarking; absorbance and steady-state microwave conductivity; Shockley-Reed-Hall lifetimes

Associated Content

Kathryn M. Neilson; Sarallah Hamtaei; Koosha Nassiri Nazif; Joshua M. Carr; Sepideh Rahimisheikh; Frederick U. Nitta; Guy Brammertz; Jeffrey L. Blackburn; Joke Hadermann; Krishna C. Saraswat; Obadiah G. Reid; Bart Vermang; Alwin Daus; Eric Pop. Toward Mass-Production of Transition Metal Dichalcogenide Solar Cells: Scalable Growth of Photovoltaic-Grade Multilayer WSe_2 by Tungsten Selenization. ArXiv. doi.org/10.48550/arXiv.2402.08534 (accessed February 13, 2024).

Acknowledgements

K.M.N. acknowledges support from the Stanford Graduate Fellowship (SGF) and from the National Science Foundation Graduate Research Fellowship (NSF-GRFP). S.H. acknowledges financial support by the

Flanders Research Foundation (FWO)—strategic basic research doctoral grant 1S31922N. K.N. acknowledges partial support from Stanford Precourt Institute for Energy and the member companies of the SystemX Alliance at Stanford. A.D. acknowledges support by the Deutsche Forschungsgemeinschaft (DFG, German Research Foundation) through the Emmy Noether Programme (506140715). Part of this work was performed at the Stanford Nano Shared Facilities (SNSF), supported by the National Science Foundation under award ECCS-2026822. Additionally, this work was authored, in part, by the National Renewable Energy Laboratory, operated by Alliance for Sustainable Energy, LLC, for the U.S. Department of Energy (DOE) under Contract No. DE-AC36-08GO28308. Microwave conductivity measurements and analysis at NREL was funded by the Solar Photochemistry Program, Division of Chemical Sciences, Geosciences, and Biosciences, Office of Basic Energy Sciences, U.S. DOE. The views expressed in the article do not necessarily represent the views of the DOE or the U.S. Government.

Author Declaration: The authors declare no competing interests.

Data Availability: The data that support the findings of this study are available from the corresponding author upon reasonable request.

References

1. Das, S.; Sebastian, A.; Pop, E.; McClellan, C. J.; Franklin, A. D.; Grasser, T.; Knobloch, T.; Illarionov, Y.; Penumatcha, A. V.; Appenzeller, J.; Chen, Z.; Zhu, W.; Asselberghs, I.; Li, L.-J.; Avci, U. E.; Bhat, N.; Anthopoulos, T. D.; Singh, R., Transistors based on two-dimensional materials for future integrated circuits. *Nature Electronics* **2021,** *4* (11), 786-799.

2. Jariwala, D.; Davoyan, A. R.; Wong, J.; Atwater, H. A., Van der Waals Materials for Atomically-Thin Photovoltaics: Promise and Outlook. *ACS Photonics* **2017,** *4* (12), 2962-2970.

3. Daus, A.; Vaziri, S.; Chen, V.; Köroğlu, Ç.; Grady, R. W.; Bailey, C. S.; Lee, H. R.; Schauble, K.; Brenner, K.; Pop, E., High-performance flexible nanoscale transistors based on transition metal dichalcogenides. *Nature Electronics* **2021,** *4* (7), 495-501.

4. Kim, K.-H.; Andreev, M.; Choi, S.; Shim, J.; Ahn, H.; Lynch, J.; Lee, T.; Lee, J.; Nazif, K. N.; Kumar, A.; Kumar, P.; Choo, H.; Jariwala, D.; Saraswat, K. C.; Park, J.-H., High-Efficiency WSe_2 Photovoltaic Devices with Electron-Selective Contacts. *ACS Nano* **2022,** *16* (6), 8827-8836.

5. Reese, M. O.; Glynn, S.; Kempe, M. D.; McGott, D. L.; Dabney, M. S.; Barnes, T. M.; Booth, S.; Feldman, D.; Haegel, N. M., Increasing markets and decreasing package weight for high-specific-power photovoltaics. *Nature Energy* **2018,** *3* (11), 1002-1012.

6. Hu, Z.; Lin, D.; Lynch, J.; Xu, K.; Jariwala, D., How good can 2D excitonic solar cells be? *Device* **2023,** *1* (1), 100003.

7. Went, C. M.; Wong, J.; Jahelka, P. R.; Kelzenberg, M.; Biswas, S.; Hunt, M. S.; Carbone, A.; Atwater, H. A., A new metal transfer process for van der Waals contacts to vertical Schottky-junction transition metal dichalcogenide photovoltaics. *Science Advances* **2019**, *5* (12), eaax6061.

8. Nassiri Nazif, K.; Nitta, F. U.; Daus, A.; Saraswat, K. C.; Pop, E., Efficiency limit of transition metal dichalcogenide solar cells. *Communications Physics* **2023,** *6* (1), 367.

9. Nassiri Nazif, K., Transition Metal Dichalcogenides for Next-Generation Photovoltaics. *Stanford University* **2021**. Online at: https://searchworks.stanford.edu/view/14053731 (accessed June 20, 2024)

10. Hou, F.; Ren, X.; Guo, H.; Ning, X.; Wang, Y.; Li, T.; Zhu, C.; Zhao, Y.; Zhang, X., Monolithic perovskite/silicon tandem solar cells: A review of the present status and solutions toward commercial application. *Nano Energy* **2024,** *124*, 109476.

11. Nassiri Nazif, K.; Daus, A.; Hong, J.; Lee, N.; Vaziri, S.; Kumar, A.; Nitta, F.; Chen, M. E.; Kananian, S.; Islam, R.; Kim, K.-H.; Park, J.-H.; Poon, A. S. Y.; Brongersma, M. L.; Pop, E.; Saraswat, K. C., High-specific-power flexible transition metal dichalcogenide solar cells. *Nature Communications* **2021,** *12* (1), 7034.

12. Nakamura, M.; Yamaguchi, K.; Kimoto, Y.; Yasaki, Y.; Kato, T.; Sugimoto, H., Cd-Free Cu(In,Ga)(Se,S)$_2$ Thin-Film Solar Cell With Record Efficiency of 23.35%. *IEEE Journal of Photovoltaics* **2019,** *9* (6), 1863-1867.

13. Huang, J.-K.; Pu, J.; Hsu, C.-L.; Chiu, M.-H.; Juang, Z.-Y.; Chang, Y.-H.; Chang, W.-H.; Iwasa, Y.; Takenobu, T.; Li, L.-J., Large-Area Synthesis of Highly Crystalline WSe_2 Monolayers and Device Applications. *ACS Nano* **2014,** *8* (1), 923-930.

14. Hynek, D. J.; Onder, E.; Hart, J. L.; Jin, G.; Wang, M.; Singhania, R. M.; Davis, B.; Strandwitz, N. C.; Cha, J. J., Substrate Effects on Growth Dynamics of WTe_2 Thin films. *Advanced Materials Interfaces* **2023,** *10* (11), 2202397.

15. Kang, H.; Yun, S. J.; Jung, K. H.; Lim, J. W., Multi-wafer-scale growth of WSe_2 films using a traveling flow-type reactor with a remote thermal Se cracker. *Applied Surface Science* **2020,** *528*, 146951.

16. Lin, W.-S.; Medina, H.; Su, T.-Y.; Lee, S.-H.; Chen, C.-W.; Chen, Y.-Z.; Manikandan, A.; Shih, Y.-C.; Yang, J.-H.; Chen, J.-H.; Wu, B.-W.; Chu, K.-W.; Chuang, F.-C.; Shieh, J.-M.; Shen, C.-H.; Chueh, Y.-L., Selection Role of Metal Oxides into Transition Metal Dichalcogenide Monolayers by a Direct Selenization Process. *ACS Applied Materials & Interfaces* **2018,** *10* (11), 9645-9652.

17. Hussain, S.; Patil, S. A.; Vikraman, D.; Arbab, A. A.; Jeong, S. H.; Kim, H.-S.; Jung, J., Growth of a WSe_2/W counter electrode by sputtering and selenization annealing for high-efficiency dye-sensitized solar cells. *Applied Surface Science* **2017,** *406*, 84-90.

18. Li, H.; Gao, D.; Xie, S.; Zou, J., Effect of magnetron sputtering parameters and stress state of W film precursors on WSe_2 layer texture by rapid selenization. *Scientific Reports* **2016,** *6* (1), 36451.

19. Morabito, F.; Synnatschke, K.; Mehew, J. D.; Varghese, S.; Sayers, C. J.; Folpini, G.; Petrozza, A.; Cerullo, G.; Tielrooij, K.-J.; Coleman, J.; Nicolosi, V.; Gadermaier, C., Long lived photogenerated charge carriers in few-layer transition metal dichalcogenides obtained from liquid phase exfoliation. *Nanoscale Advances* **2024**.

20. Jäger-Waldau, A.; Bucher, E., WSe_2 thin films prepared by soft selenization. *Thin Solid Films* **1991,** *200* (1), 157-164.

21. Hei, J.; Li, X.; Wu, S.; Lin, P.; Shi, Z.; Tian, Y.; Li, X.; Zeng, L.; Yu, X.; Wu, D., Wafer-Scale Patterning Synthesis of Two-Dimensional WSe_2 Layers by Direct Selenization for Highly Sensitive van der Waals Heterojunction Broadband Photodetectors. *ACS Applied Materials & Interfaces* **2023,** *15* (9), 12052-12060.

22. Aftab, S.; Iqbal, M. Z.; Hussain, S.; Hegazy, H. H.; Saeed, M. A., Transition metal dichalcogenides solar cells and integration with perovskites. *Nano Energy* **2023,** *108*, 108249.

23. Hamtaei, S.; Brammertz, G.; Kohl, T.; Buldu, D. G.; Birant, G.; de Wild, J.; Meuris, M.; Poortmans, J.; Vermang, B., Investigating the experimental space for two-step $Cu(In,Ga)(S,Se)_2$ absorber layer fabrication: A design of experiment approach. *Thin Solid Films* **2021,** *738*, 138958.

24. Vleuten, M. v. d.; Theelen, M.; Aninat, R.; Werf, K. v. d.; Mannetje, H.; Reyes-Figueroa, P.; Kodalle, T.; Klenk, R.; Simor, M.; Linden, H. In *Control over the Gallium Depth Profile in 30×30 cm^2 Sequentially Processed CIGS*, 2020 47th IEEE Photovoltaic Specialists Conference (PVSC), 15 June-21 Aug. 2020; 2020; pp 0640-0645.

25. Zeng, W.; Feng, L.-P.; Su, J.; Pan, H.-x.; Liu, Z.-T., Layer-controlled and atomically thin WS2 films prepared by sulfurization of atomic-layer-deposited WO_3 films. *Journal of Alloys and Compounds* **2018,** *745*, 834-839.

26. Zhou, D.; Shu, H.; Hu, C.; Jiang, L.; Liang, P.; Chen, X., Unveiling the Growth Mechanism of MoS_2 with Chemical Vapor Deposition: From Two-Dimensional Planar Nucleation to Self-Seeding Nucleation. *Crystal Growth & Design* **2018,** *18* (2), 1012-1019.

27. Schutte, W. J.; De Boer, J. L.; Jellinek, F., Crystal structures of tungsten disulfide and diselenide. *Journal of Solid State Chemistry* **1987,** *70* (2), 207-209.

28. Patterson, A. L., The Scherrer Formula for X-Ray Particle Size Determination. *Physical Review* **1939,** *56* (10), 978-982.

29. del Corro, E.; Terrones, H.; Elias, A.; Fantini, C.; Feng, S.; Nguyen, M. A.; Mallouk, T. E.; Terrones, M.; Pimenta, M. A., Excited Excitonic States in 1L, 2L, 3L, and Bulk WSe_2 Observed by Resonant Raman Spectroscopy. *ACS Nano* **2014,** *8* (9), 9629-9635.

30. Qian, Q.; Peng, L.; Perea-Lopez, N.; Fujisawa, K.; Zhang, K.; Zhang, X.; Choudhury, T. H.; Redwing, J. M.; Terrones, M.; Ma, X.; Huang, S., Defect creation in WSe2 with a microsecond photoluminescence lifetime by focused ion beam irradiation. *Nanoscale* **2020,** *12* (3), 2047-2056.

31. Dadgar, A. M.; Scullion, D.; Kang, K.; Esposito, D.; Yang, E. H.; Herman, I. P.; Pimenta, M. A.; Santos, E. J. G.; Pasupathy, A. N., Strain Engineering and Raman Spectroscopy of Monolayer Transition Metal Dichalcogenides. *Chemistry of Materials* **2018,** *30* (15), 5148-5155.

32. Reid, O. G.; Moore, D. T.; Li, Z.; Zhao, D.; Yan, Y.; Zhu, K.; Rumbles, G., Quantitative analysis of time-resolved microwave conductivity data. *Journal of Physics D: Applied Physics* **2017,** *50* (49), 493002.

33. Labram, J. G.; Perry, E. E.; Venkatesan, N. R.; Chabinyc, M. L., Steady-state microwave conductivity reveals mobility-lifetime product in methylammonium lead iodide. *Applied Physics Letters* **2018,** *113* (15), 153902.

34. Blackburn, J. L.; Zhang, H.; Myers, A. R.; Dunklin, J. R.; Coffey, D. C.; Hirsch, R. N.; Vigil-Fowler, D.; Yun, S. J.; Cho, B. W.; Lee, Y. H.; Miller, E. M.; Rumbles, G.; Reid, O. G., Measuring Photoexcited Free Charge Carriers in Mono- to Few-Layer Transition-Metal Dichalcogenides with Steady-State Microwave Conductivity. *The Journal of Physical Chemistry Letters* **2020,** *11* (1), 99-107.

35. Bindl, D. J.; Ferguson, A. J.; Wu, M.-Y.; Kopidakis, N.; Blackburn, J. L.; Arnold, M. S., Free Carrier Generation and Recombination in Polymer-Wrapped Semiconducting Carbon Nanotube Films and Heterojunctions. *The Journal of Physical Chemistry Letters* **2013,** *4* (21), 3550-3559.

36. Park, J.; Reid, O. G.; Rumbles, G., Photoinduced Carrier Generation and Recombination Dynamics of a Trilayer Cascade Heterojunction Composed of Poly(3-hexylthiophene), Titanyl Phthalocyanine, and C60. *The Journal of Physical Chemistry B* **2015,** *119* (24), 7729-7739.

37. Ferguson, A. J.; Kopidakis, N.; Shaheen, S. E.; Rumbles, G., Dark Carriers, Trapping, and Activation Control of Carrier Recombination in Neat P3HT and P3HT:PCBM Blends. *The Journal of Physical Chemistry C* **2011,** *115* (46), 23134-23148.

38. Ihly, R.; Mistry, K. S.; Ferguson, A. J.; Clikeman, T. T.; Larson, B. W.; Reid, O.; Boltalina, O. V.; Strauss, S. H.; Rumbles, G.; Blackburn, J. L., Tuning the driving force for exciton dissociation in single-walled carbon nanotube heterojunctions. *Nature Chemistry* **2016,** *8* (6), 603-609.

39. Li, Y.; Chernikov, A.; Zhang, X.; Rigosi, A.; Hill, H. M.; van der Zande, A. M.; Chenet, D. A.; Shih, E.-M.; Hone, J.; Heinz, T. F., Measurement of the optical dielectric function of monolayer transition-metal dichalcogenides: MoS_2, $MoSe_2$, WS_2 and WSe_2. *Physical Review B* **2014,** *90* (20), 205422.

40. Dicker, G.; de Haas, M. P.; Siebbeles, L. D. A.; Warman, J. M., Electrodeless time-resolved microwave conductivity study of charge-carrier photogeneration in regioregular poly(3-hexylthiophene) thin films. *Physical Review B* **2004,** *70* (4), 045203.

41. Ferguson, A. J.; Kopidakis, N.; Shaheen, S. E.; Rumbles, G., Quenching of Excitons by Holes in Poly(3-hexylthiophene) Films. *The Journal of Physical Chemistry C* **2008,** *112* (26), 9865-9871.

42. Ando, Y.; Khatri, I.; Matsumori, H.; Sugiyama, M.; Nakada, T., Epitaxial Cu(In,Ga)Se2 Thin Films on Mo Back Contact for Solar Cells. *physica status solidi (a)* **2019,** *216* (16), 1900164.

43. Ochoa, M.; Buecheler, S.; Tiwari, A. N.; Carron, R., Challenges and opportunities for an efficiency boost of next generation Cu(In,Ga)Se_2 solar cells: prospects for a paradigm shift. *Energy & Environmental Science* **2020,** *13* (7), 2047-2055.

44. Ablekim, T.; Duenow, J. N.; Perkins, C. L.; Moseley, J.; Zheng, X.; Bidaud, T.; Frouin, B.; Collin, S.; Reese, M. O.; Amarasinghe, M.; Colegrove, E.; Johnston, S.; Metzger, W. K., Exceeding 200 ns Lifetimes in Polycrystalline CdTe Solar Cells. *Solar RRL* **2021,** *5* (8), 2100173.

45. Jakubowicz, A.; Mahalu, D.; Wolf, M.; Wold, A.; Tenne, R., WSe_2: Optical and electrical properties as related to surface passivation of recombination centers. *Physical Review B* **1989,** *40* (5), 2992-3000.